



A redundantly actuated 2-DOF 3RRR PKM with flexure joints: less is more

Dustin Berendsen¹ · Aditya Sridhar¹ · Ronald Aarts¹ 

Received: 31 March 2022 / Accepted: 23 March 2023
© The Author(s) 2023

Abstract

The development of a planar manipulator with flexure joints and redundant actuation has been considered before, showing that the redundancy can be exploited to increase the support stiffness and to reduce static actuator loads. In this previous design the manipulator's workspace has been defined to encompass all kinematically accessible end effector positions. In the current paper we reconsider the design philosophy. It will be shown that limiting the workspace (“less”) ultimately results in a better performance in a larger area (“more”).

The dynamic performance of the manipulator is evaluated with a flexible multibody model. The links can safely be considered as rigid parts, but the model has to account for the nonlinear stiffness behaviour of the flexure joints undergoing relatively large deflections. The nonlinear spatial flexible beam elements implemented in the SPACAR software result in numerically efficient models that have proven to be well-suited for design optimisation. With such a flexible multibody model, the geometry of the manipulator is optimised to maximise the workspace area while assuring a minimal parasitic natural frequency and limiting the local stresses throughout the full workspace. Furthermore, the simulations show that preloading of the flexure joints results in reduced actuator torques that are needed to counteract the finite joint compliance for stationary positioning anywhere except for the equilibrium position of the end effector.

The optimised design has been build and validated experimentally. A control system that handles the actuator redundancy by minimising the 2-norm of the driving torques has been synthesised. It is demonstrated that the setup's behaviour is similar to the model and that in particular the preloading significantly lowers the required actuator torques.

Keywords Flexure-based mechanisms · Redundantly actuated parallel kinematic manipulator (PKM) · Nonlinear beam elements · Experimental system identification · Actuator torque balancing

1 Introduction

In [1] a redundantly actuated 2-DOF 3RRR parallel kinematic manipulator (PKM) with flexure joints (Fig. 1(a)) has been introduced as “best of both worlds” for precision applica-

✉ R. Aarts
r.g.k.m.aarts@utwente.nl

¹ Faculty of Engineering Technology, Applied Mechanics & Data Analysis, University of Twente, P.O. Box 217, 7500 AE Enschede, The Netherlands

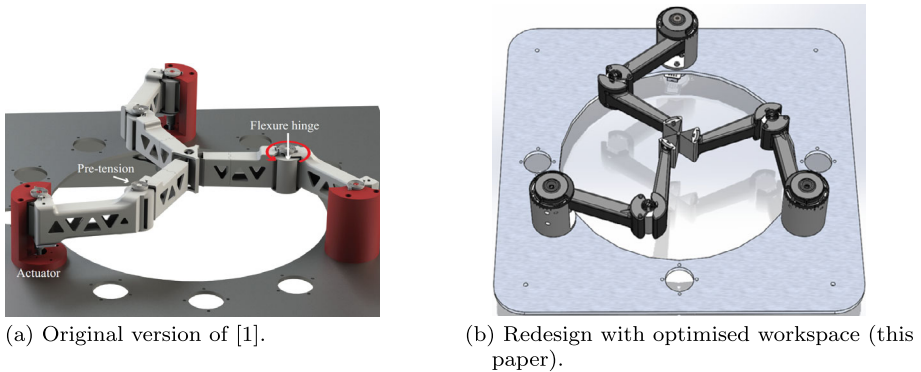


Fig. 1 Designs of planar 2-DOF 3RRR PKM with compliant (or flexure) joints

tions. Using flexure joints deterministic behaviour can be realised because of the low level of friction, hysteresis and backlash [9, 16]. Being also a redundantly actuated PKM, it combines the advantages of PKM, i.e. the high stiffness, low inertia and large accelerations, with an improved handling of singularities and optimised actuator loading made possible by the redundancy [12, 14]. Simulations indeed demonstrated advantages of combining both concepts. The flexure hinges in compliant manipulators inherently show a reduced support stiffness for large joint angles. In a PKM with one or more redundant links, this reduction can be limited. Furthermore, the redundant actuation offers a possibility to combine load balancing techniques with preloading of the compliant joints to reduce the actuator efforts needed to keep the end effector (EE) stationary at any position different from the equilibrium position [1, 2].

A PKM with “classical” joints is typically operated throughout the complete kinematically admissible range [13]. Mimicking this behaviour with flexure joints is a challenge in view of the required joint angles. Originally, the range of motion for flexure joints was limited to rotation of a few degrees. In recent years, more advanced joint concepts emerged [15] that allow rotations in the order of $\pm 45^\circ$. Nevertheless, the inevitable build up of internal stress and the decrease of the support stiffness at large deflections reduce the effective operational range of the hinges. Hence we investigate in this paper how a similar performance can be obtained throughout the same or even larger workspace area as before (“more”) when the joint angles are limited (“less”). This can be accomplished by using longer links, which come with the drawback of an increased mass resulting in lower unwanted natural frequencies. The longer links can still be beneficial if the larger mass is compensated by an increased support stiffness due to less required joint rotations. The optimisation of this trade-off is presented in this paper as well as an experimental validation. For this purpose, a setup that aims to be a proof of concept to demonstrate the most relevant properties in terms of natural frequencies and required actuator torques has been build.

2 Design optimisation

In this section, the steps involved in the mechatronic design of the manipulator are addressed. At first, a relatively simple low-order kinematic and dynamic model is used. In Sect. 2.1 the main kinematic properties are outlined. The 2-DOF equation of motion is formulated in Sect. 2.2 and used in Sect. 2.3 to evaluate the stiffness balancing with preloaded

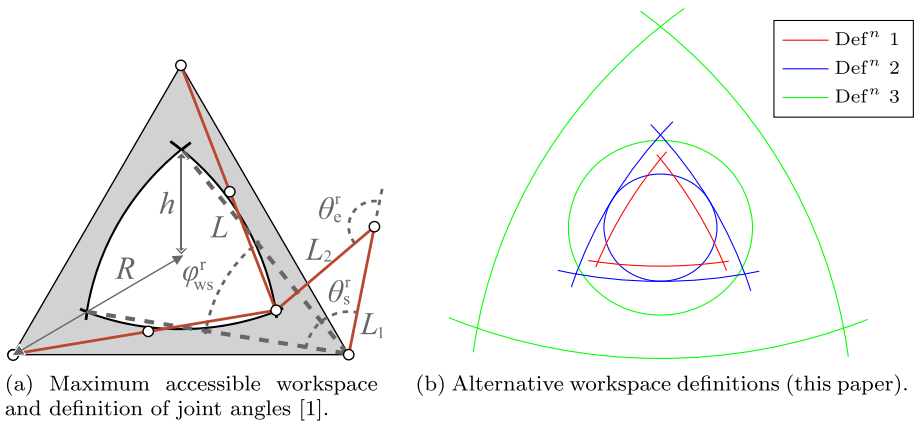


Fig. 2 Workspace definitions. (Colour figure online)

joints. Basically this concludes the low-order modelling of the manipulator, which is used in Sect. 2.4 to propose a controller for position feedback control that can handle the actuator redundancy.

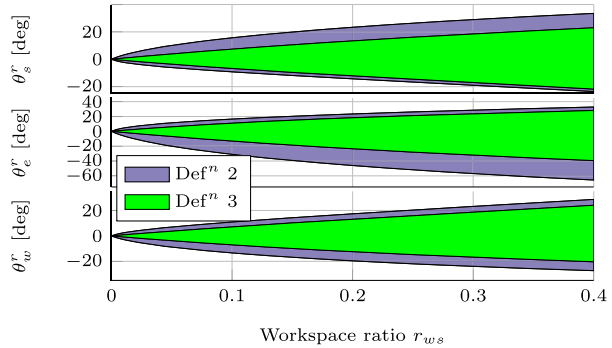
The achievable performance of the feedback controller is directly linked to its closed-loop bandwidth [5], which in turn is limited by so-called parasitic natural frequencies. These frequencies can be understood from a flexible multibody model of the manipulator. Being a 2-DOF system, there will be two relatively low natural frequencies associated with the manipulator motion according to these two DOF. These frequencies can be computed from the low-order model of Sect. 2.2, which only depends on a few lumped system parameters like link masses and joint rotational stiffnesses. The parasitic natural frequencies result from any other mode shape the manipulator can exhibit. To simulate this behaviour, a more advanced model is needed. To develop this model, first the selection of favourable flexure joint types is addressed in Sect. 2.5. Next, the geometrical parameters that describe the manipulator can be defined, with which a parametric flexible multibody model of the manipulator is built in Sect. 2.6. Then, finally, the optimisation procedure is proposed in Sect. 2.7.

2.1 Kinematic analysis and definitions of the workspace

The three arms of the 3RRR PKM are assumed to be similar, and the actuators are located at the corners of an equilateral triangle, see Figs. 1 and 2(a). At first, a simplified kinematic model is used to determine the reachable workspace and the required joint rotations. The rigid links are connected with ideal rotational joints. Two important geometrical parameters are the total length L of each arm and the distance R of each actuator to the centre of the triangle. The workspace reachable by the EE is bounded by three circular arcs with radii L , of which an example is shown in red and labelled “Defⁿ 1” in Fig. 2(b). This is the workspace that has been considered in [1]. The worst case dynamic performance is found in the corners of this area where two arms are fully stretched. In these locations the support stiffness will be lowest as several joints are at or close to their extreme rotation angles.

The blue curves, labelled “Defⁿ 2”, in Fig. 2(b) present a first alternative workspace definition. Instead of trying to move to all reachable locations, the corners are cut off, e.g. by limiting the workspace to the enclosed blue circle. It can be shown that using longer arms, i.e. larger L , and restricting the joint rotations, a larger workspace area can be reached

Fig. 3 Rotation ranges of the joints



with the same ratio between mass and support stiffness as before [17]. Although this is an improvement, it appeared that for controlled EE motion still difficulties arose from singular behaviour near the three locations on the enclosed circle where one of the arms is fully stretched.

Hence a third definition of the workspace is presented with the green curves, labelled “Defⁿ 3”, in Fig. 2(b). This workspace is a circle that is some fixed offset radius R_o smaller than the maximum enclosed circle such that the (near) singularities are avoided. This results in even more reduced ranges of the rotations for the joints as presented in Fig. 3. The joint angles in this figure are computed for a manipulator where the total arm length L is split into equal halves for the upper and lower arm, respectively. The three figures show the required ranges of motion for the shoulder (θ_s^r), elbow (θ_e^r) and wrist (θ_w^r) joints, respectively. These ranges of motion are illustrated in Fig. 2(a) for the maximum workspace of “Defⁿ 1”, but are smaller for the two workspace definitions shown in Fig. 3. The required rotational ranges are presented as functions of the so-called (linear) workspace ratio, which is defined as

$$r_{ws} = \sqrt{A_{ws}/A_{fp}}, \tag{1}$$

where A_{ws} is the workspace area and A_{fp} is the triangular area of the manipulator’s footprint. It can be seen that the third definition of the workspace requires smaller joint angles to reach the same area. A drawback is that the arm length increases even more compared to “Defⁿ 2”, which could result in less support stiffness as will be examined in the dynamic analysis of Sect. 2.6.

2.2 2-DOF dynamic model

A low order 2-DOF model is derived first. It should capture the main low frequent dynamic behaviour and will be used for the control synthesis. The low order model can be obtained relatively straightforwardly, e.g. using the Euler–Lagrange equation for the kinematic model of Sect. 2.1 supplemented with (link) masses and (joint) rotational stiffnesses. The result can be expressed in the usual way as

$$\bar{\mathbf{M}}(\mathbf{q})\ddot{\mathbf{q}} + \mathbf{C}(\mathbf{q}, \dot{\mathbf{q}})\dot{\mathbf{q}} + \mathbf{Q}(\mathbf{q}) = \mathbf{A}^T(\mathbf{q})\boldsymbol{\tau}, \tag{2}$$

where \mathbf{q} are the two independent coordinates for which it is convenient to take the EE coordinates x_{ee} and y_{ee} . Matrix $\bar{\mathbf{M}}$ is the configuration dependent (reduced) mass matrix; \mathbf{C} accounts for the Coriolis terms; \mathbf{Q} represents the (nonlinear) stiffness contributions and the transpose of the Jacobian matrix \mathbf{A} transforms the three actuator torques $\boldsymbol{\tau}$ into effective forces on the EE.

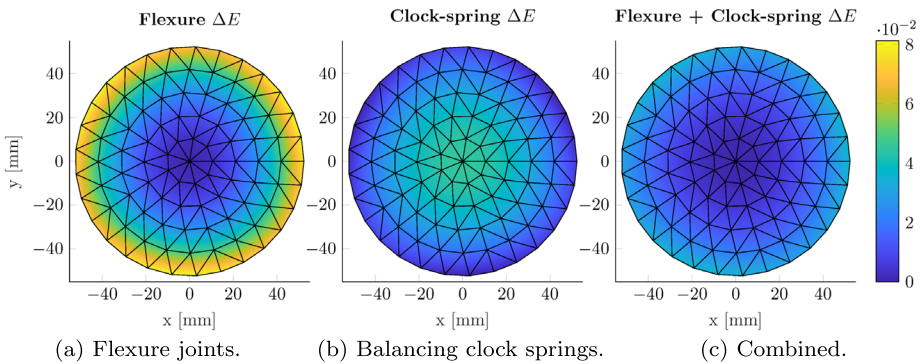


Fig. 4 Potential energy (in J) stored in the flexure joints (left), balancing clock springs (middle) and combined (right)

2.3 Stiffness balancing with preloaded joints

The term \mathbf{Q} in Eq. (2) is directly linked to the finite stiffness of the flexure joints for their rotation in the in-plane compliant direction. In the neutral configuration of the manipulator with the EE in the centre, this term is zero. To position the EE at locations near the extremity of the workspace, this term can be quite large and even result in actuator saturation making these locations unreachable. Lowering the stiffness is mostly not possible as a reduced stiffness in the compliant direction typically also results in an undesirable reduced support stiffness. However, as outlined in [1, 2], preloading of the joints can result in lower required actuator torques. Such preloading can be implemented by installing flexure joints that are already rotated in the neutral configuration, or alternatively by adding preloaded clock springs in parallel to the flexure joint.

A quick way to evaluate the effectiveness of these clock springs follows from an analysis of the stored potential energy. Knowing the kinematic configuration of the manipulator, Sect. 2.1, the potential energy stored in all flexure joints can be computed as a function of the EE position, see Fig. 4(a). With zero potential energy in the neutral configuration, the energy stored increases towards the boundary of the workspace.

Similarly, the energy stored in the preloaded clock springs can be evaluated. It appears that this energy can decrease when moving towards the boundary with adequate settings for preload and stiffness [2]. Figure 4(b) shows an example where the minimum energy level in the workspace is arbitrarily set to zero. This energy distribution can be manipulated by using clock springs with a different stiffness and by varying the preload. More details on the clock springs are given in Sect. 2.7.

Combining these plots gives Fig. 4(c), which illustrates that for the manipulator with these balancing clock springs still some positive stiffness is observed, but significantly less compared to the unbalanced case. In this way it will be possible to reach the full workspace with reduced actuator torques.

2.4 Controller synthesis

Reconsidering the equation of motion (2), it can be seen that any specific motion can be accomplished by applying the effective force on the EE as follows from the right-hand side of this equation. In other words, the actuator torques should be such that the term $\mathbf{A}^T(\mathbf{q})\boldsymbol{\tau}$

equals the left-hand side of this equation. Because of the redundant actuation, there is no unique solution. Let us consider, for example, the stationary positioning of the manipulator, in which case only the stiffness has to be handled, i.e.

$$\mathbf{A}^T(\mathbf{q})\boldsymbol{\tau} = \mathbf{Q}(\mathbf{q}). \quad (3)$$

From this equation it can be seen that knowing one valid solution for $\boldsymbol{\tau}$, all other solutions can be found by adding any vector from the null space of the Jacobian matrix \mathbf{A}^T . A common procedure is to select the set of torques $\boldsymbol{\tau}$ that minimise a specific norm. Considering the 2-norm, the solution equals

$$\boldsymbol{\tau} = (\mathbf{A}^T(\mathbf{q}))^\dagger \mathbf{Q}(\mathbf{q}), \quad (4)$$

where $()^\dagger$ indicates the (Moore–Penrose) pseudo-inverse of the matrix [8].

It can be noted that in view of possible actuator saturation, the use of the ∞ -norm [19] is more adequate as this minimises the largest required actuator torque. However, it was found that the benefit from this norm was relatively small and hence the simpler computation of the 2-norm will be implemented in the setup.

For controlled motion, the required effective EE force is generated by a control system, where feedback and feedforward control can be combined. Feedforward makes use of system knowledge by evaluating the equation of motion (2) to compute a feedforward force in real-time for a prescribed trajectory $(\mathbf{q}, \dot{\mathbf{q}}, \ddot{\mathbf{q}})$. Relevant parameters of the manipulator need to be estimated. In this paper only relatively slow motions are considered, and hence only stiffness feedforward will be applied, i.e. Eq. (3).

In addition, feedback control is used to account for model inaccuracies in the feedforward control and disturbances. PID-control will be implemented following the approach of [5].

2.5 Parametric model

As pointed out at the start of this section, the achievable control bandwidth in general depends strongly on the parasitic natural frequencies of the manipulator. To simulate these frequencies, the 2-DOF model of Sect. 2.2 does not suffice, and a more elaborate flexible multibody model is developed in the next section. For such a model, the joint concepts have to be detailed first and their relevant dimensional parameters are defined.

In the previous design [1], the shoulder and elbow joint are butterfly joints, see Fig. 5 [7]. This joint type is used at the shoulder location for its small pivot shift compared to many other flexure joints. This is also favourable in the current design as at the shoulder the rotation is driven by a motor with a fixed rotational axis.

For the elbow joint, it is essential that the flexure can handle rather large rotations as can be seen in Fig. 3. Although other, more complex joint types [15] may offer a larger range of motion, the butterfly hinge is considered to be adequate for the present proof of concept of the manipulator.

In the previous design, the basic working principle of the butterfly hinge was also used in the wrist joint to connect the three arms. A disadvantage is the need of an intermediate body that can give rise to an additional rotational DOF at the EE, which can result in unwanted parasitic vibrations or even loss of the redundancy. Hence a so-called tri-cartwheel joint, see Fig. 6, is proposed for this connection. This hinge shows a larger pivot shift, and more stresses will occur in the deformed leaf springs, but for the considered range of motion this appears to be acceptable.

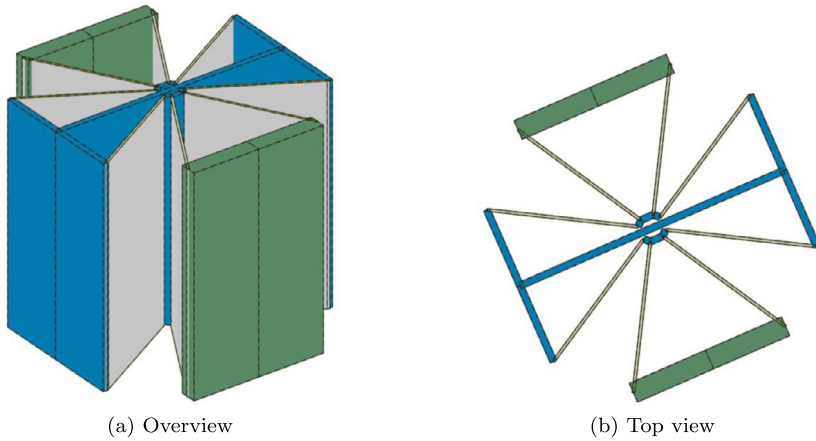


Fig. 5 Schematic representation of the butterfly joint. The grey parts are the deformable leaf springs. Both rigid connections for the links are green and the rigid intermediate body is coloured blue. (Colour figure online)

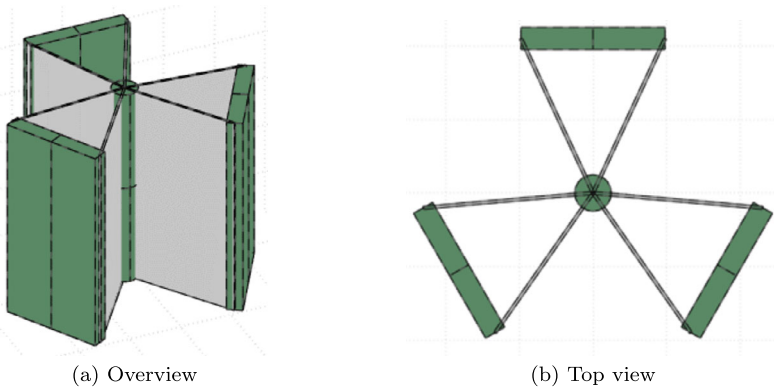


Fig. 6 Schematic representation of the tri-cartwheel joint. The grey parts are the deformable leaf springs. The green parts are all rigid representing three connections for the links and the connection between all flexure parts in the centre, which is also the location of the end effector. (Colour figure online)

For design optimisation, the overall model of the manipulator with the joints is expressed in a set of parameters, see Fig. 7. To limit the computer time needed for the optimisation, the number of parameters is limited to a reasonable number as will be explained next. Some parameters are fixed by design, or it is known beforehand that some extreme value is the most likely outcome, see Table 1(a). Table 1(b) lists the varying parameters with lower and upper bounds.

At manipulator level, the link lengths and the location of the actuators strongly affect the workspace ratio, as defined in Eq. (1). The radius R at which the actuators are positioned, see Fig. 7(a), is fixed to the value used in [1]. The link lengths L_1 and L_2 of upper and lower arm, respectively, are taken identical and are described by a single design variable, the length ratio L_r defined as

$$L_r = \frac{L}{R} = \frac{L_1 + L_2}{R} = \frac{2L_1}{R} = \frac{2L_2}{R}. \quad (5)$$

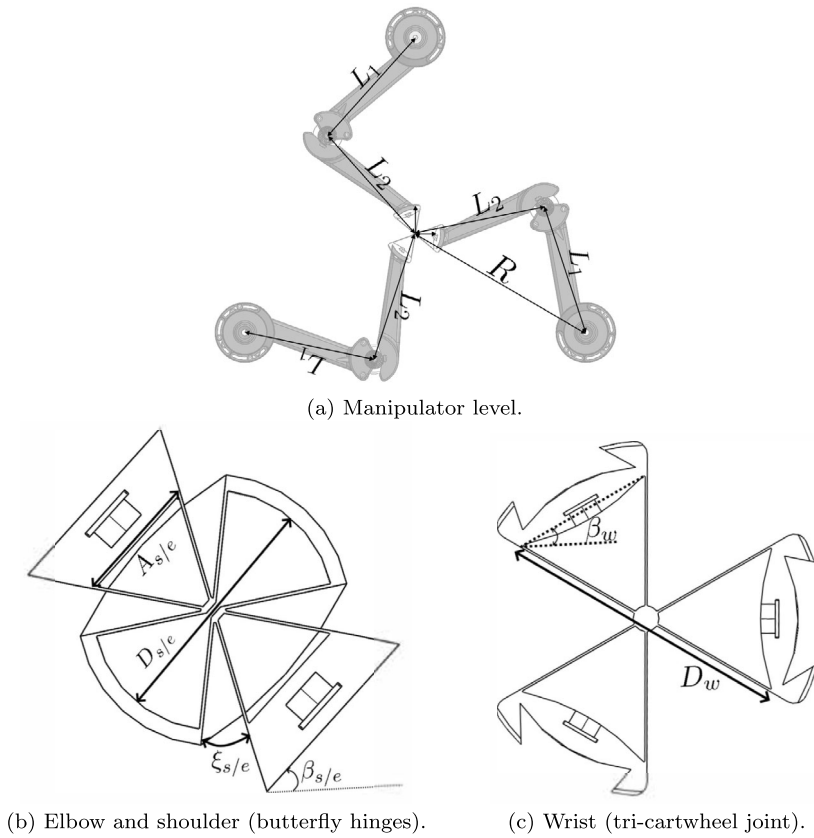
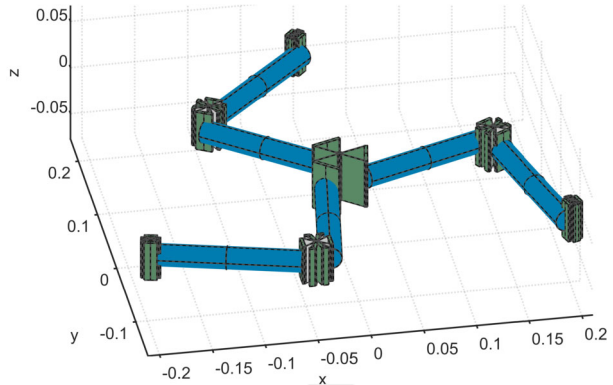


Fig. 7 Design parameters

Table 1 Design parameters of the 3RRR PKM, as defined in Fig. 7

(a) Fixed parameters			(b) Variable parameters with lower bound (lb), upper bound (ub) and optimal value (opt, Sect. 2.7).				
Parameter	Value	Unit	Parameter	lb	ub	opt	Unit
ξ_s	22.5	deg	A_s	9	20	12.0	mm
ξ_e	30	deg	D_s	10	60	16.9	mm
R	230.5	mm	A_e	9	20	15.9	mm
t	0.4	mm	D_e	10	60	30.5	mm
$h_{s/e}$	40	mm	D_w	10	60	56.4	mm
h_w	50	mm	L_r	1.1	1.8	1.34	
			β_s	-90	0	-0.1	deg
			β_e	-90	0	-71.3	deg
			β_w	-30	30	20.0	deg
			R_o	0	50	25.9	mm

Fig. 8 SPACAR multibody model of the redundantly actuated flexure based 3RRR PKM



This length ratio L_r is varied within reasonable bounds. A final parameter at manipulator level affecting the (effective) workspace is the offset radius R_o that was introduced to exclude singularities from the workspace labelled “Def” 3” in Fig. 2(b). This radius can vary from zero, i.e. effectively the workspace defined as “Def” 2”, to about a quarter of the (maximum) length of the links (L_1 or L_2).

At hinge level, the leaf springs are characterised by their length, width h and thickness t . The latter two dimensions are fixed for all joints. It is known that the thickness t of the leaf springs tends to be minimised as it reduces stress build-up without affecting the support stiffness too much. Its value will be motivated in Sect. 2.7. The width h is the out-of-plane dimension of the hinges in Figs. 7(b) and (c). It is fixed to the values listed in Table 1(a).

For the optimal performance of the butterfly hinges for both shoulder and elbow joints, it has been found that the clearance angles ξ_s and ξ_e as indicated in Fig. 7(b) need to be minimised [18]. Hence these angles are fixed to the minimal estimated required clearance angle for the expected range of motion.

Finally, the stiffness properties of the joints depend on the other dimensions listed in Table 1(b) and on the hinge orientation angles β_s , β_e and β_w . These angles describe the respective hinge orientations from a global point of view, see Figs. 7(b) and (c).

2.6 Flexible multibody model and parasitic natural frequencies

The manipulator as outlined in the previous section, see, for example, Fig. 7(a), is modelled to evaluate and optimise its dynamic properties, especially in terms of required actuator torques and natural frequencies. For this purpose, a flexible multibody model of the manipulator has been defined in the SPACAR software package [11]. In this model the manipulator is composed of rigid and flexible spatial beam elements, see Fig. 8. The links of the manipulator and intermediate bodies in the flexure joints are modelled with rigid beams, basically describing the mass and inertia properties. All leaf springs are modelled with nonlinear flexible beam elements in which all six deformation modes are considered to be flexible, i.e. elongation, torsion and bending in both directions. This has been proven to be an accurate and efficient approach [1, 15, 18]. In particular, the nonlinear stiffness in all directions is evaluated accurately with a rather small number of elements even for leaf springs undergoing relatively large deflections. Stiffening due to constraint warping is included as it may be significant for the wide and short leaf springs in the joints [10].

The relevant dynamic properties of the manipulator model in Fig. 8 are evaluated in the neutral configuration and with the EE positioned at the edge of the workspace with maximum displacements in negative and positive y direction. From an analysis of its behaviour

in the complete workspace, it is known that these positions are most critical for actuator requirements, stress limits and drop in parasitic natural frequencies.

The mechanical model does not immediately reveal the optimal actuator torques. Instead, one of the possible solutions is found and Eq. (4) is used to compute the 2-norm optimal actuator torques. The natural frequencies and accompanying mode shapes follow from an eigenvalue analysis of the mass and stiffness matrices of locally linearised models in the three considered EE positions. The lowest parasitic natural frequency found in this way is considered in the optimisation to be outlined next.

2.7 Design optimisation

Ideally, metal flexures and bearingless motors should be used for a high performance manipulator. As pointed out in the introduction, the system considered in this paper should mainly be a proof of concept to demonstrate the main expected characteristics of a redundantly actuated PKM with flexure joints. High accuracy and high performance are not the main targets at this stage. Then the basic control scheme of Sect. 2.4 suffices and relatively low-cost manufacturing techniques can be used. More specifically, the mechanical components of the demonstrator are realised with 3D printing. Some larger parts are printed in PLA with the FDM process, which is relatively cheap. The flexure hinges require a higher accuracy and lower tolerances for the thin leaf springs and are printed in nylon with the SLS process. Using this material, it is not possible to apply preloading by installing flexure joints that are already rotated in the neutral configuration as they will quickly unload due to relaxation. For that reason, preloaded clock springs are mounted in parallel to the flexure joint, as was also suggested in Sect. 2.3. Furthermore, direct-drive rotational motors are used to actuate the system, although the bearings in these motors to some extent sacrifice the otherwise fully compliant behaviour of the manipulator.

The aim of the design optimisation is to achieve an improved performance compared to the previous manipulator shown in Fig. 1(a) [1]. Such improvement concerns unwanted parasitic natural frequencies, maximum stress in the deformed flexures, range of motion, manipulator dimensions, required actuator torques or any combination of these criteria and possibly even more. If multiple of these aspects are optimised simultaneously, their relative weighting has to be specified. For a fair comparison between new and previous designs, it is not trivial to define the weighting factors. Hence the optimisation focusses on enlarging the workspace of the manipulator for fixed outer dimensions and with constraints that assure the parasitic natural frequencies are at least as high as previously [1] and that stress limits are satisfied.

Taking these considerations into account, the workspace for the test-setup is optimised for the parametric model outlined in Sect. 2.5. The fixed value for the flexure thickness of $t = 0.4$ mm in Table 1(a) is close to the minimal thickness that can be printed reliably with used SLS process. Ten design parameters have been defined in Table 1(b). Material properties are given in Table 2 for the materials and parts introduced above. Table 3 lists the constraints. The first constraint imposes that the stresses remain below the maximum allowable stress, Table 2, with a safety factor of 1.5. The next constraints require the parasitic natural frequencies to be at least as high as in the previous design [1], as explained above. The remaining constraints take the actuator limits into account. The upper arms are actuated with Maxon EC45 Flat 70 W motors that offer a maximum nominal torque of 0.128 Nm.

The MATLAB script `fminsearchcon` is used for the optimisation. It implements a direct search method where nonlinear inequality constraints are included by means of a penalty function [4]. As the goal is to obtain the maximum workspace, the inverse of the

Table 2 Material and parts properties of the test setup

Material	Property	Value	Unit
PolyLactic Acid (PLA)	Tensile strength	45	MPa
	Young's modulus	3.5	GPa
	Density	1250	kg/m ³
Nylon PA2200 [6]	Tensile strength	45	MPa
	Young's modulus	1.7	GPa
	Density	930	kg/m ³
Clock springs			
Lesjöfors SCS 0.5 × 3 × 5 [3]	Stiffness	0.0321	Nm/rad

Table 3 Nonlinear inequality constraints

Property	Value	Unit
Maximum stress	≤ 30	MPa
First parasitic eigenfrequency	≥ 45	Hz
Second parasitic eigenfrequency	≥ 50	Hz
Balanced driving torque	≤ 0.1	Nm
Non-balanced driving torque	≤ 0.4	Nm

workspace ratio r_{ws} of Eq. (1) is minimised. The constraints for the natural frequencies and stresses are evaluated in the neutral configuration and in the two critical EE locations on the border of the workspace, as explained in Sect. 2.6.

The obtained optimal values for the parameters are included in Table 1, and a CAD model of the manipulator is shown in Fig. 1(b). Figure 9(a) illustrates the first natural frequency throughout the workspace. Clearly, it satisfies the constraint. Similarly, Fig. 9(b) shows that the second natural frequency is well above the constraint in the workspace. It can be verified that the other constraints are not violated either. The parasitic natural frequencies do not vary much, which shows that the support stiffness remains rather constant. The accompanying first vibration mode in the neutral configuration is presented in Fig. 9(c), from which it is clear that this is an out-of-plane vibration.

Evaluating the optimised design, it appears that it results in a further increase of the workspace area while the first simulated parasitic natural frequency is kept above 45 Hz. More specifically, the workspace ratios as shown in Fig. 2(b) are respectively $r_{ws} = 0.1922$ in the original “Defⁿ 1” (red) [1], $r_{ws} = 0.2167$ for “Defⁿ 2” (blue) [17], but it can now be increased to $r_{ws} = 0.3532$ (green).

Finally, it should be noted that the driving torque constraint in Table 3 can also be met. For the selected clock spring (Table 2), it was found that optimal balancing of the driving torques is obtained when the clock springs in the shoulders and elbows are preloaded by mounting these springs with initial deflection angles of 233° and −120°, respectively.

3 Experimental results

The redundantly actuated manipulator with flexure joints described and designed in the previous section has been built to be able to validate the expected dynamic behaviour exper-

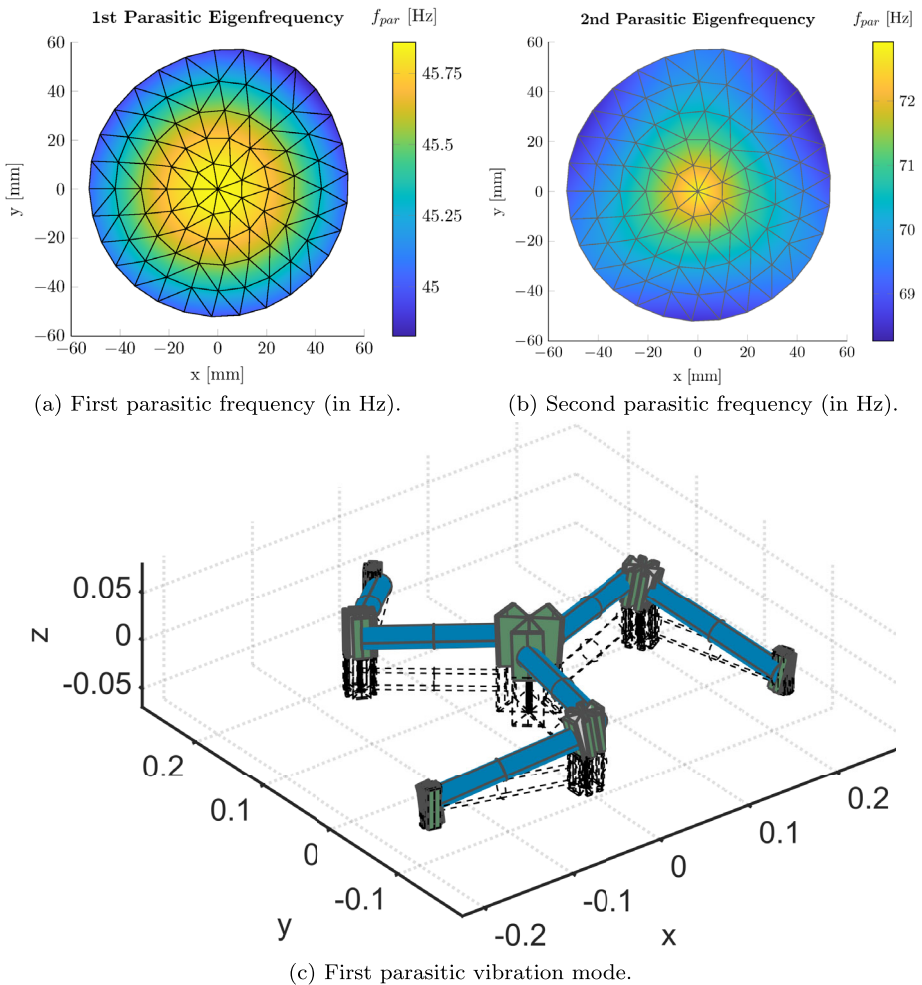


Fig. 9 First and second parasitic frequencies and mode

imentally. This applies in particular to the (parasitic) natural frequencies, which will be concluded from the estimated frequency response function in Sect. 3.1. It should be noted that even though high accuracy was not a goal for the proof of concept of the manipulator, some basic controller tuning is needed to be able to move the manipulator through its workspace, Sects. 3.2 and 3.3. With this motion, the required actuator torques are measured, as presented in Sect. 3.4.

3.1 System identification

The dynamic behaviour of the actual manipulator has been characterised with system identification where a multi-sine excitation is used to estimate the frequency response of Fig. 10. In agreement with the equation of motion (2), the redundant actuation and the sensing of the motor torques and rotations are transformed to two degrees of freedom being both in-plane forces F_x , F_y and translations x_{ee} , y_{ee} of the EE. This experiment is performed at 14

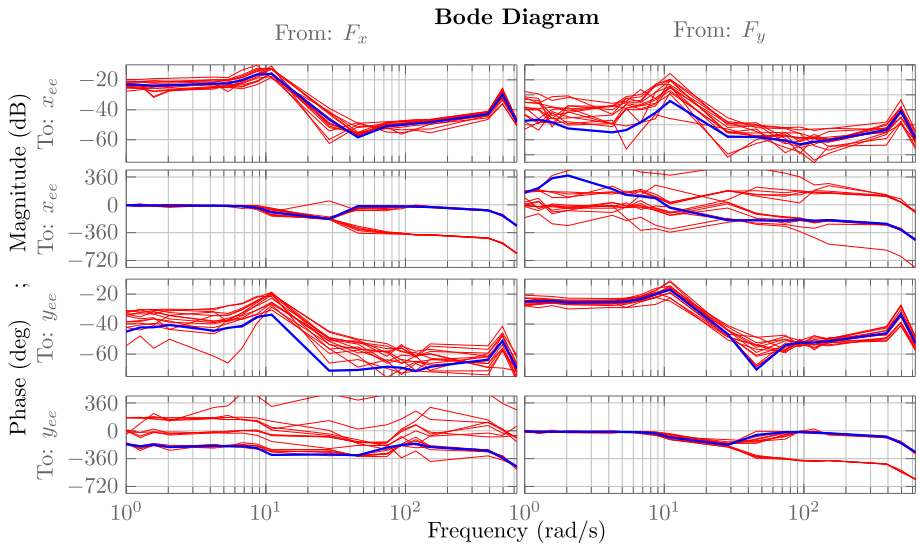


Fig. 10 Identified frequency response functions (FRF) in 14 different EE locations (red) and average (blue). (Colour figure online)

locations in the workspace (red curves). The blue curves indicate averages of these measurements.

In the theoretical equation of motion, the translations in x and y directions of the EE near the neutral configuration can be modelled as decoupled motions. In the FRF plots, this is confirmed as the diagonal terms are larger than the off-diagonal cross-coupling terms.

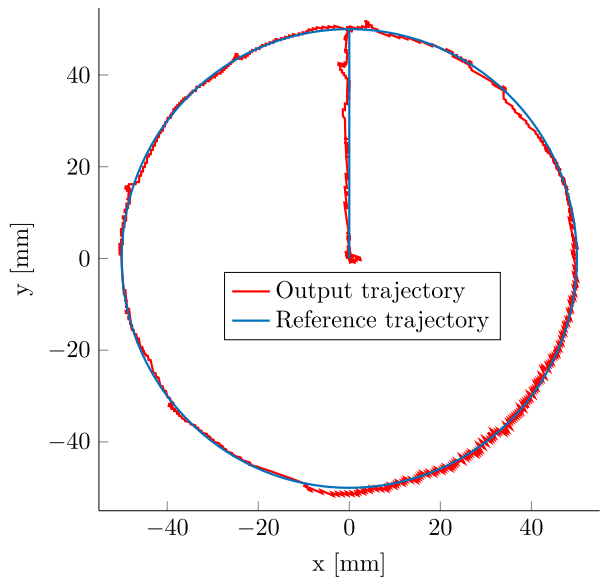
The first parasitic natural frequency appears to be about 500 rad/s or 80 Hz. This frequency is higher than expected in Sect. 2.7. A possible cause could be a larger stiffness. Manufacturing tolerances can result in a slightly different thickness of the leaf springs that strongly affects the stiffness properties. Additionally, the model does not account for flexible shaft couplings that are installed between the actuators and upper arms.

The higher natural frequency could be beneficial for the controller stability. Unfortunately, the FRF plots also show an anti-resonance (or zero pair in the transfer function) near 30 rad/s or 5 Hz. Even worse, in some of the FRF curves this zero pair is combined with a phase lag of -180° instead of the usual phase lead of $+180^\circ$, which indicates these are non-minimum phase zeros. Such zeros will make it hard or impossible to achieve a high control bandwidth. Although these anti-resonances and accompanying zeros can be simulated in the SPACAR models, their existence was not included in the design optimisation.

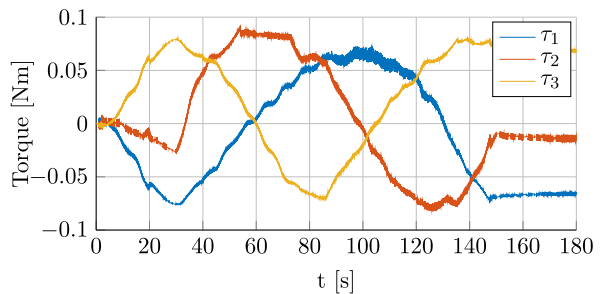
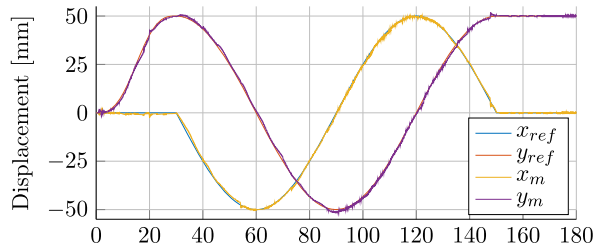
3.2 Controller tuning

The observation in the previous section of a mainly diagonal plant can be used to apply a diagonal controller as well. In this way the settings of the PID-controller are found quite straightforwardly [5]. However, to handle the destabilising effects from the anti-resonances described in the previous section, the PID-controller is supplemented with a notch filter. Setting the filter frequency at about 495 rad/s or 79 Hz, a stable closed-loop system could be obtained with an open-loop crossover frequency of about 18 rad/s or 3 Hz.

Fig. 11 Tracking of a circular reference path. (Colour figure online)



(a) Output trajectory vs. reference trajectory.



(b) Required actuator torques.

3.3 Reference tracking

To demonstrate the controlled motion of the EE, a circular reference trajectory is defined close to the boundary of the workspace, see Fig. 11(a). An initial linear segment is added to move the EE from the neutral configuration to the circle. The actual motion is included in the plot. It shows reasonable tracking accuracy with some occasional small spikes. These may be caused by cogging effects of the (direct-drive) motors or other disturbances that are only weakly suppressed as the controller bandwidth is rather limited. Also noticeable is

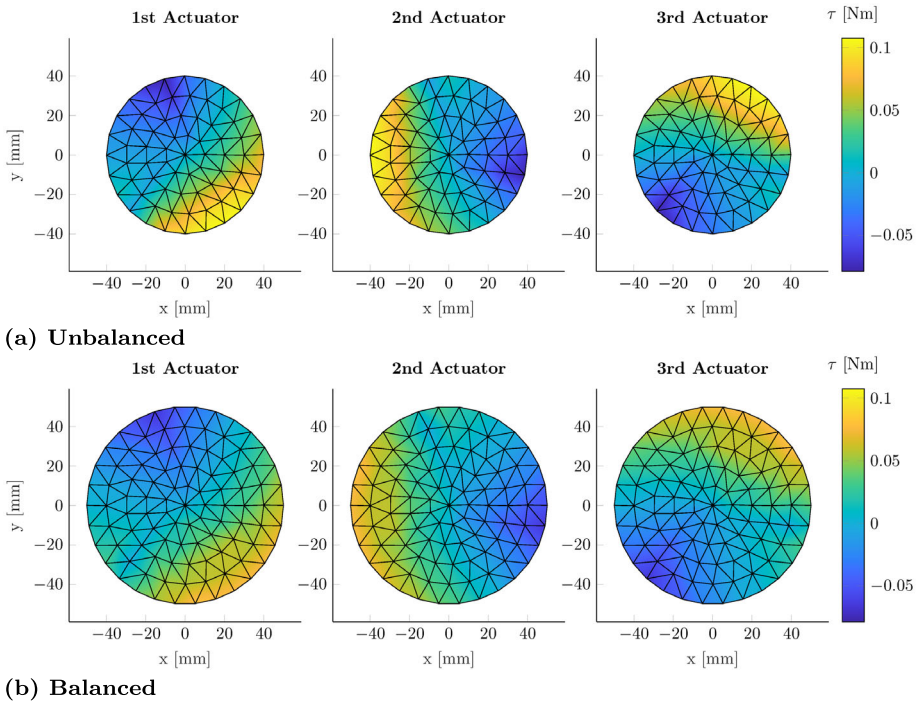


Fig. 12 Experimentally determined actuator torques for the unbalanced (a/top) and balanced (b/bottom) manipulator

an increased noise level in the lower right corner of the circle. This is due to quantisation noise of the digital encoders that measure the rotation with a resolution of 512 lines per revolution, so 2048 counts per revolution. In this experiment only two encoders were used, which results in an output singularity in this region. This can be avoided by exploiting the redundant sensing. Figure 11(b) presents the actuator torques during the motion, which will be discussed in more detail next.

3.4 Stiffness balancing

As outlined in Sect. 2.3, the preloading of the flexure joints plays an important role in reducing the actuator torques needed to cope with the stiffness of the joints. The balancing of the actuator torques is investigated by positioning the EE throughout the workspace with and without preloading of elbow and shoulder joints. Figure 12(b) shows that with preloading the maximum torques of all actuators stay well within the imposed limit. Without this preloading, it can be seen in Fig. 12(a) that the torque limits are already exceeded before the edges of the workspace are reached. Hence only a smaller area is shown.

4 Conclusion

This paper shows a new design approach for a planar 2-DOF 3RRR parallel manipulator with redundant actuation and compliant joints, i.e. flexure joints. The goal was to maximise

the workspace area in which a similar or better performance could be realised as before [1] in terms of the first parasitic natural frequency. It turned out to be beneficial to limit the workspace to an area that avoids (near) singular manipulator configurations. In this way the ranges for the joint rotations are restricted so that the joint support stiffnesses of the deformed flexures are reduced less. This allows for the use of longer link lengths, which in the end results in a significant increase of the workspace area. In addition, a new concept is proposed for the wrist joint connecting the three arms in the end effector. A flexible multibody model has been built where the leaf springs in the flexure joints are modelled with the nonlinear beam elements of the SPACAR software. The parameters in this model have been optimised to obtain the largest workspace area while satisfying constraints regarding the parasitic natural frequencies, local stresses and actuator limits.

A hardware implementation of this manipulator has been realised. Although the mechanical parts of this setup have been manufactured with relatively low-cost 3D printing, it demonstrates some of the main features like the sufficiently high parasitic natural frequency. However, it also appeared that the closed-loop performance is considerably limited by the existence of anti-resonances or transfer function zeros that could have been predicted by the SPACAR flexible multibody models, but were not taken into account during the design. A further increase of the workspace area could result from applying a more advanced joint type for the elbow joints allowing larger rotations. For true high performance, the flexure hinges should be manufactured from different material like metal. Also, the use of frictionless actuators, like pure torque motors, should be considered. Attention should be paid to using sufficiently accurate sensors and taking advantage of the sensor redundancy. Finally, to handle higher velocities, the stiffness or position dependent feedforward control should be supplemented with the acceleration, velocity and position dependent inertia effects of the equation of motion (2). These improvements will be considered in future research where also in-plane rotation of the end effector will be added as a third DOF to a redundantly actuated PKM in order to increase the practical applicability of this type of manipulators.

The setup in particular proved that preloading of the shoulder and elbow joints results in a significant reduction of the required actuator torques in agreement with the modelled prediction.

Declarations

Competing Interests The authors declare that they have no conflict of interest.

Open Access This article is licensed under a Creative Commons Attribution 4.0 International License, which permits use, sharing, adaptation, distribution and reproduction in any medium or format, as long as you give appropriate credit to the original author(s) and the source, provide a link to the Creative Commons licence, and indicate if changes were made. The images or other third party material in this article are included in the article's Creative Commons licence, unless indicated otherwise in a credit line to the material. If material is not included in the article's Creative Commons licence and your intended use is not permitted by statutory regulation or exceeds the permitted use, you will need to obtain permission directly from the copyright holder. To view a copy of this licence, visit <http://creativecommons.org/licenses/by/4.0/>.

References

1. Cornelissen, R., Müller, A., Aarts, R.: A compliant and redundantly actuated 2-DOF 3RRR PKM: best of both worlds? In: Kecskeméthy, A., Flores, F.G. (eds.) *Multibody Dynamics 2019*, pp. 163–171. Springer, Cham (2020). https://doi.org/10.1007/978-3-030-23132-3_20
2. de Jong, J.J., Aarts, R.G.: Static balance of a flexure-based four-bar mechanism: less torque with more preload. In: *Proceedings of the 31st International Conference on Robotics in Alpe-Adria-Danube Region, RAAD2022*. Klagenfurt am Wörthersee, Austria (2022). 8 pages

3. De Spiraal: SCS $0.5 \times 3 \times 5$ (2021). <https://stocksprings.despiraal.nl/product/711601-scs-0-5x3x5>. Accessed: November 2021
4. D'Errico, J.: *fminsearchbnd*, *fminsearchcon* – on MATLAB Central File Exchange (2006). <https://www.mathworks.com/matlabcentral/fileexchange/8277-fminsearchbnd-fminsearchcon>. Accessed: September 2020
5. Dijk, J., Aarts, R.: Analytical one parameter method for PID motion controller settings. *IFAC Proc.* Vol. **45**(3), 223–228 (2012). <https://doi.org/10.3182/20120328-3-IT-3014.00038>
6. EOS GmbH Electro Optical Systems: Fine polyamide PA 2200 for EOSINT P (2010). <https://www.sculpteo.com/media/data/faq/pa2200-datasheet.pdf>. Accessed: November 2021
7. Henein, S.: Short communication: flexure delicacies. *Mech. Sci.* **3**(1), 1–4 (2012). <https://doi.org/10.5194/ms-3-1-2012>
8. Hollerbach, J., Suh, K.: Redundancy resolution of manipulators through torque optimization. *IEEE J. Robot. Autom.* **3**(4), 308–316 (1987). <https://doi.org/10.1109/JRA.1987.1087111>
9. Howell, L.L., Magleby, S.P., Olsen, B.M.: *Handbook of Compliant Mechanisms*. Wiley, New York (2013). ISBN 978-1-119-95345-6
10. Jonker, J.B.: Three-dimensional beam element for pre- and post-buckling analysis of thin-walled beams in multibody systems. *Multibody Syst. Dyn.* **52**(1), 59–93 (2021). <https://doi.org/10.1007/s11044-021-09777-x>
11. Jonker, J.B., Meijaard, J.P.: SPACAR – computer program for dynamic analysis of flexible spatial mechanisms and manipulators. In: Schiehlen, W. (ed.) *Multibody Systems Handbook*, pp. 123–143. Springer, Berlin (1990). https://doi.org/10.1007/978-3-642-50995-7_9
12. Kock, S., Schumacher, W.: A parallel x-y manipulator with actuation redundancy for high-speed and active-stiffness applications. In: *Proceedings of the 1998 IEEE International Conference on Robotics and Automation*, Leuven, Belgium, vol. 3, pp. 2295–2300 (1998). <https://doi.org/10.1109/ROBOT.1998.680665>
13. Krajoski, K., Müller, A., Gattringer, H., Jörgl, M.: Design, modeling and control of an experimental redundantly actuated parallel platform. In: Niel, K., Roth, P. (eds.) *Proceedings of the OAGM&ARW Joint Workshop 2016 “Computer Vision and Robotics”*, pp. 209–216. University of Applied Sciences Upper Austria, Wels Campus (2016). <https://doi.org/10.3217/978-3-85125-528-7-29>
14. Müller, A., Hufnagel, T.: Model-based control of redundantly actuated parallel manipulators in redundant coordinates. *Robot. Auton. Syst.* **60**(4), 563–571 (2012). <https://doi.org/10.1016/j.robot.2011.11.014>
15. Naves, M., Brouwer, D., Aarts, R.: Building block-based spatial topology synthesis method for large-stroke flexure hinges. *J. Mech. Robot.* **9**(4), 041,006 (2017). <https://doi.org/10.1115/1.4036223> (9 pages)
16. Soemers, H.: *Design Principles for Precision Mechanisms*. T-Point Print VoF, Enschede (2011). ISBN 978-90-365-3103-0
17. Sridhar, A.: *Workspace optimisation and motion control of a redundant flexural 2-DoF 3RRR parallel kinematic manipulator*. Master's thesis, University of Twente, Enschede, The Netherlands (2020)
18. Wiersma, D.H., Boer, S.E., Aarts, R.G.K.M., Brouwer, D.M.: Design and performance optimization of large stroke spatial flexures. *J. Comput. Nonlinear Dyn.* **9**(1), 011,016 (2013). <https://doi.org/10.1115/1.4025669> (10 pages)
19. Woo, S.H., Kim, S.M., Kim, M.G., Yi, B.J., Kim, W.: Torque-balancing algorithm for the redundantly actuated parallel mechanism. *Mechatronics* **42**, 41–51 (2017). <https://doi.org/10.1016/j.mechatronics.2017.01.002>

Publisher's Note Springer Nature remains neutral with regard to jurisdictional claims in published maps and institutional affiliations.